Star Flats for DECam

(V2 / Work in Progress)

Nicolas Regnault*

LPNHE (Paris)

February 22, 2013

The relative variations of the response of DECam as a function of focal plane position, can be studied from sequences of dithered images of dense stellar fields. Several such sequences were observed in november and december 2012, during the commissioning of DECam. We present preliminary maps derived from these observations. They display radial non-uniformities (3 to 5%, center to edge), which are significantly larger than what is expected from plate scale variations alone. In the g and z bands, they also display ring-shaped structures of about 2% in intensity. Potential variations of the edges of the DECam filters were also tested. Small ($< 1\%$) but measurable effects were detected in the r, i and z bands. More work is required to 1) check these results, with at least one additional epoch 2) understand the structure of the star flats from the DECal observations.

Contents

1 Introduction **3**

2 Dataset **3**

3 Photometry pipeline **4**

3.1 Preprocessing 4

3.2 Photometry 5

4 "Gray" Star flats **5**

4.1 Model 5

4.2 Results 6

*nicolas.regnault@lpnhe.in2p3.fr

5 Testing for Filter Uniformity **10**
5.1 The model 10
5.2 Field star colors 10
5.3 Results 11

6 Stability of the dithering sequence **16**
6.1 IQ Variations 16
6.2 Variations of the atmospheric absorption 16

7 Stability of the star flat solution **18**

8 Work ahead **21**

1 Introduction

The subject of this note is discussed in detail in §2 of (Betoule et al., 2012, hereafter B12), as well as §4 and appendix A of (Regnault et al., 2009, hereafter R09). Briefly, the photometry of point sources delivered by a wide-field imager after flatfielding is generally not uniform at the level of a few percents. Many effects contribute to these non-uniformities: plate scale variations, variations of the filter normalization and filter edges as a function of position, pollution of the flatfield frames by stray light and ghosts, QE variations from chip to chip, gain variations from amplifier to amplifier... T

The idea is to take dithered observations of well-chosen, dense stellar fields, and measure how the instrumental flux of stars vary as a function of focal plane position (assuming that the observing conditions are stable). From this, it is possible to derive maps that encode the variations of the imager response. These maps may then be integrated to the flatfields, or one may rather choose to use them at a later stage of the processing, for example, to correct directly the object fluxes in the catalogs.

Two dithered sequences have been taken during DECam commissioning and pre-survey time, in the griz- and Y-bands. In what follows, we report on a preliminary analysis of this dataset. We briefly present the data in §2. The aspects of the photometry pipeline that may differ from the standard DES pipeline are discussed in §3. The star flats derived from both sequences are then presented in sections 4 and 5.

2 Dataset

The dataset is presented in table 1. Two fields were observed in the 5 DECam bands g,r,i,z and Y (no u-band observations), one in November 2012, and another one about a month later. Each sequence comprises about 20 exposures per field and per band. The December sequences are longer, as two centered control exposures are taken, in order to check for the stability of the observing conditions.

The dithering pattern is logarithmic, allowing to probe for the small and large scale variations of the response map. Figure 1 shows the offsets that were applied to the images. They are similar, and seem to differ by one rotation, for reasons that are unclear to me.

Table 1: Star flat observations.

date	RA (J2000)	DEC (J2000)	bands	# exposures / band
2012-11-20	06:40:04.091	-34:00:02.5	gri	20
2012-11-21	"	"	zY	“
2012-12-22	07:30:05.440	-49:59:47.7	grizY	22

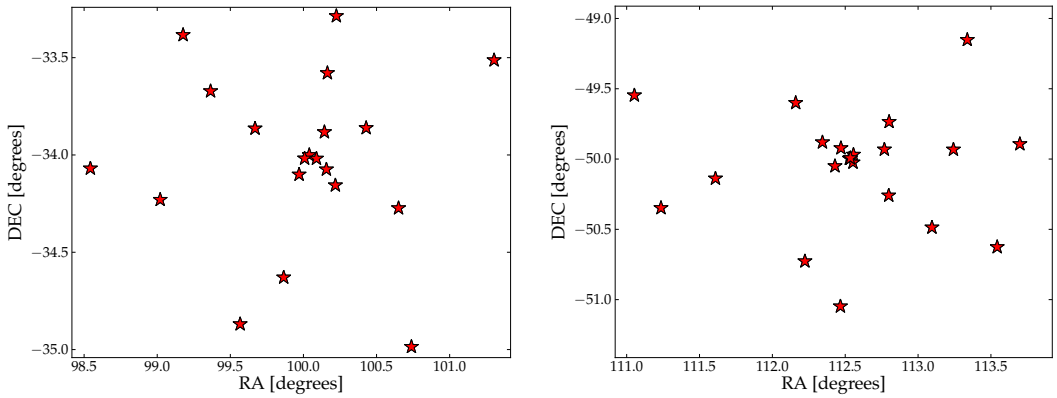

(a) November field.

(b) December field.

Figure 1: Dithering patterns applied to the November and December star flat sequences.

3 Photometry pipeline

The SNLS photometry pipeline was adapted to be able to process the 62-ccd DES exposures. We started the processing from scratch (i.e. raw pixels, flatfields and bias frames). Roughly, the pipeline implements the following operations: 1) build a master bias frame and master flat fields (median stacks), 2) split the images into CCDs, 3) subtract a bias frame and apply the median flatfield, 4) map and subtract the sky background, detect and measure the objects (this intermediate processing step is done using a modified version sextractor), 5) compute weight maps and dead pixel maps, 6) Remeasure the gaussian moments and positions of all objects, identify the stars (from their moments), estimate their aperture fluxes, 7) refine the WCS transformations, using the USNO catalog a reference. This photometry pipeline is described in detail in B12 and R09. In what follows, we discuss two points that may have an impact on the star flats we derive from the data: the flatfielding procedure, and the star flux estimator.

3.1 Preprocessing

Master bias frames were constructed by taking the median of approximately 10 bias exposures taken on the same night. These bias frames were subtracted from the science exposures, taking into account potential variations of an overall pedestal level from the overscan region:

$$\text{Exposure}(i,j) = \text{Raw}(i,j) - \text{Bias}(i,j) + \text{corr} \tag{1}$$

where corr is the median of the difference between the raw frame overscan and the bias overscan.

Master flat frames were constructed using in a similar way. For each CCD, a median stack was constructed. Although we are dealing with dome flats, which do not display

significant variations from exposure to exposure, we choose to renormalize each CCD frame before computing the median stack. Then, since we have altered the relative normalization of the various amplifiers, we have to re-normalize the master flat, in order to preserve the relative levels of each amplifier. (What we do is that we compute the average levels of the amplifiers, relative to one, chosen as a reference, and then, we multiply the master flat by those quantities).

3.2 Photometry

The flux estimator is described in sections 4.1 and 4.2 of R09. For each star we compute a series of aperture fluxes in radii which are a function of image quality. The image quality is estimated independently on each CCD, by measuring the gaussian moments of all objects, isolating the stellar-like objects, and computing the average moments of these stars. All the maps described below have been obtained using apertures of radius: $r \sim 7.5 \times \mathrm{HWHM} \sim 14$ pixels.

The image IQ seems to be uniform, as a function of focal plane position, hence, we do not expect significant non-uniformities from the flux estimator itself. However, it would be safe to compare the star flats obtained with different photometry algorithms. Indeed, the star flats are sensitive to all the features of the flux estimator that may translate into position dependent biases of the photometry.

4 "Gray" Star flats

4.1 Model

We start with the simplest model possible: a correction independent of the star colors. This model is summarized in the equation below:

$$m_{\mathrm{ADU}|\mathbf{x}} = m_{\mathrm{ADU}|\mathbf{x}_0} + \delta\mathrm{zp}(\mathbf{x}) \tag{2}$$

where $m_{\mathrm{ADU}|\mathbf{x}}$ is the measured star flux and $m_{\mathrm{ADU}|\mathbf{x}_0}$ is the flux of the same star if it were observed at some reference location $\mathbf{x}_0$ on the focal plane. $\delta\mathrm{zp}(\mathbf{x})$ is the star flat we are trying to determine. By construction, $\delta\mathrm{zp}(\mathbf{x}_0) = 0$.

Since we do not know anything *a priori* on the star flats, we first choose to parametrize them using independent super-pixels. This solution has the other advantage that it also captures possible amplifier to amplifier gain variations that have not been absorbed by the flat-fielding procedure (e.g. if the gains have varied between the flat field and the science exposures). In a second step, once we know more about the star flats, it will be possible to use a well-chosen smooth function.

Given the density of the fields, we decide to use 1024×1024 super-pixels, which permits to accumulate between 3000 (g-band) to 9000 (in r and i) measurements for each super-pixel. This yields 4 parameters per amplifier, hence 496 parameters (actually 495, since one of the super-pixels is taken as a reference, and its value is fixed at 0).

The instrumental magnitudes of the stars at the reference location, $m_{\mathrm{ADU}|\mathbf{x}_0}$ must also be considered as parameters, since most stars are not observed at this location.

date	band	N_{meas}	$N_{\text{superpixels}}$	$N_\star$	χ^2/N_{dof}
2012-11-20	g	1,695,740	496	259,623	8.12
2012-11-20	r	1,308,745	496	244,819	7.32
2012-11-20	i	1,046,012	496	215,175	7.86
2012-11-21	z	2,055,479	496	362,207	2.48
2012-11-21	Y	1,474,661	496	254,928	2.61
2012-12-22	g	1,518,975	496	221,088	3.11
2012-12-22	r	2,461,799	496	368,714	3.29
2012-12-22	i	4,471,541	496	563,979	2.61
2012-12-22	z	3,613,081	496	525,538	2.10
2012-12-22	Y	2,717,598	496	394,033	2.24

Table 2: grizY star flats (no color terms).

This adds a considerable number of parameters to the problem (a few 10^5, see table 2). Fortunately, one can take advantage of the sparsity of the jacobian matrix and obtain the exact solution to the fit, as described in appendix A of R09.

4.2 Results

The model above has been fitted independently on each sequence. The fit consists in a series of independent χ^2 minimizations, interlaced with outlier rejection sequences. On average, about 60 outliers per superpixel (i.e. 2% of all measurements) are identified and rejected.

The fit results are summarized in table 2 and figures 2, 3, 8. Table 2 reports 1) the number of valid measurements, for each sequence, 2) the number of superpixels, 3) the total number of field stars (which count as nuisance parameters), and 4) the reduced χ^2 at the end of the fit. The high reduced χ^2 obtained on `2012-11-20` are attributed to instabilities of the observing conditions. The following sequences seem to be much better behaved. They show that our uncertainties are slightly under-estimated. (We should probably add an additional flat-field uncertainty. Also, I have not updated the gains after flatfielding. This will be corrected in the next iteration of this note.)

We notice that in all bands (except the Y where the CCD-to-CCD quantum efficiency variations start to dominate), all star flats exhibit quasi-radial patterns. On the largest scales, we see a smooth 5% (peak-to-peak, center-to-edge) pattern which is essentially identical in all bands. Then, the second important feature is a ring-like structure, around the center of the focal plane. The intensity and shape of this structure depends on the band. It is sharp and clearly apparent in g and z, and smoother in r and i.

These maps should be interpreted as follows. A star observed on a side of the focal plane will appear about 5% *brighter* than when it is observed at the center of the imager. Similarly, a star observed at the position of the ring-like structure will appear about 2% *fainter* than if it where observed at the center.

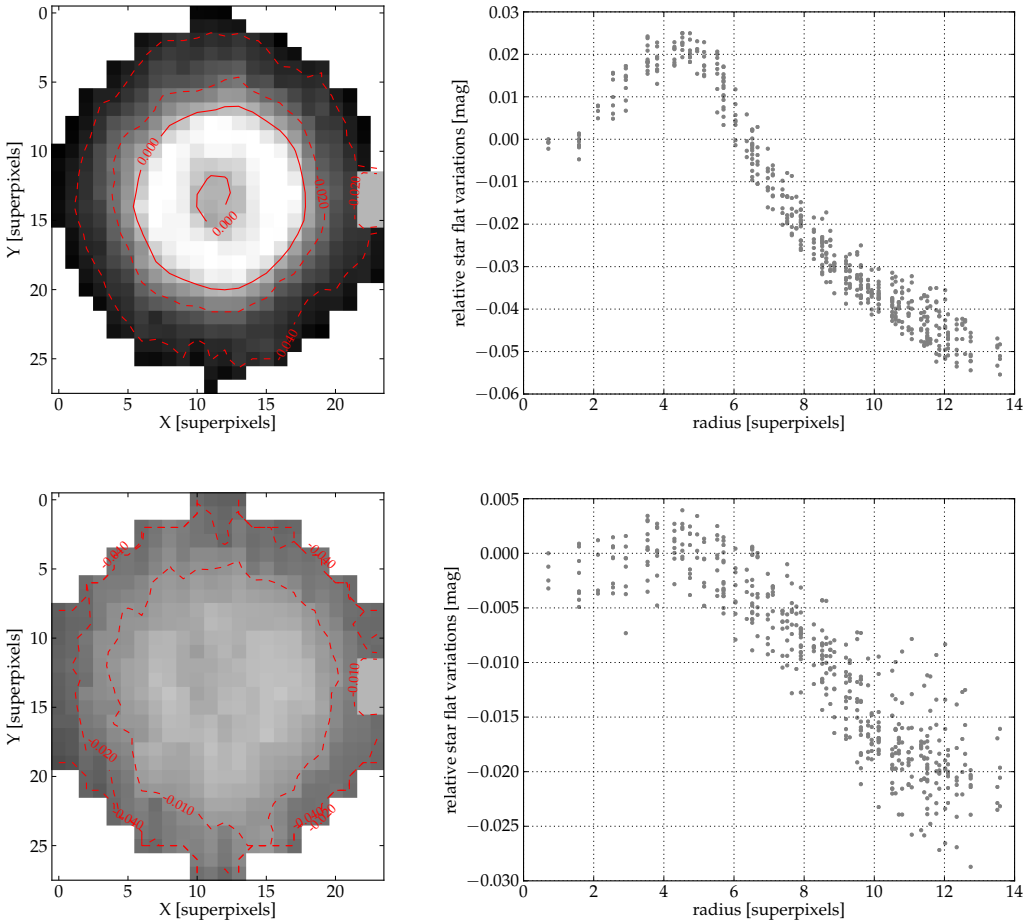

Figure 2: g-band (up) and r-band (down) star flats (2012-12-22)

Plate scale variations and ghost contamination of the flat fields are the two most obvious candidates that come into mind when trying to interpret these star flats.

The plate scale variations are easy to quantify once we have a series of exposures with reliable WCS transformations. Actually, the quantity that interests us is the solid angle subtended by a pixel (and its variations). Indeed, the pixels that are on the side of the camera subtend a fraction of sky which is smaller by a a few percent compared to what is seen by the pixels at the center of the focal plane. Hence, even if the dome illumination were perfectly uniform, the flat-field frames should integrate a few percent less flux per on the side than at the center. On the other hand, this does not affect point sources. Therefore, we expect that, on flat-fielded images, the measured star fluxes will reflect the flat-field non-uniformity.

The lower panel of figure 4 displays a map of relative variations of the pixel solid angle. As can be seen, the DECam plate scale seems to be remarkably uniform over the focal

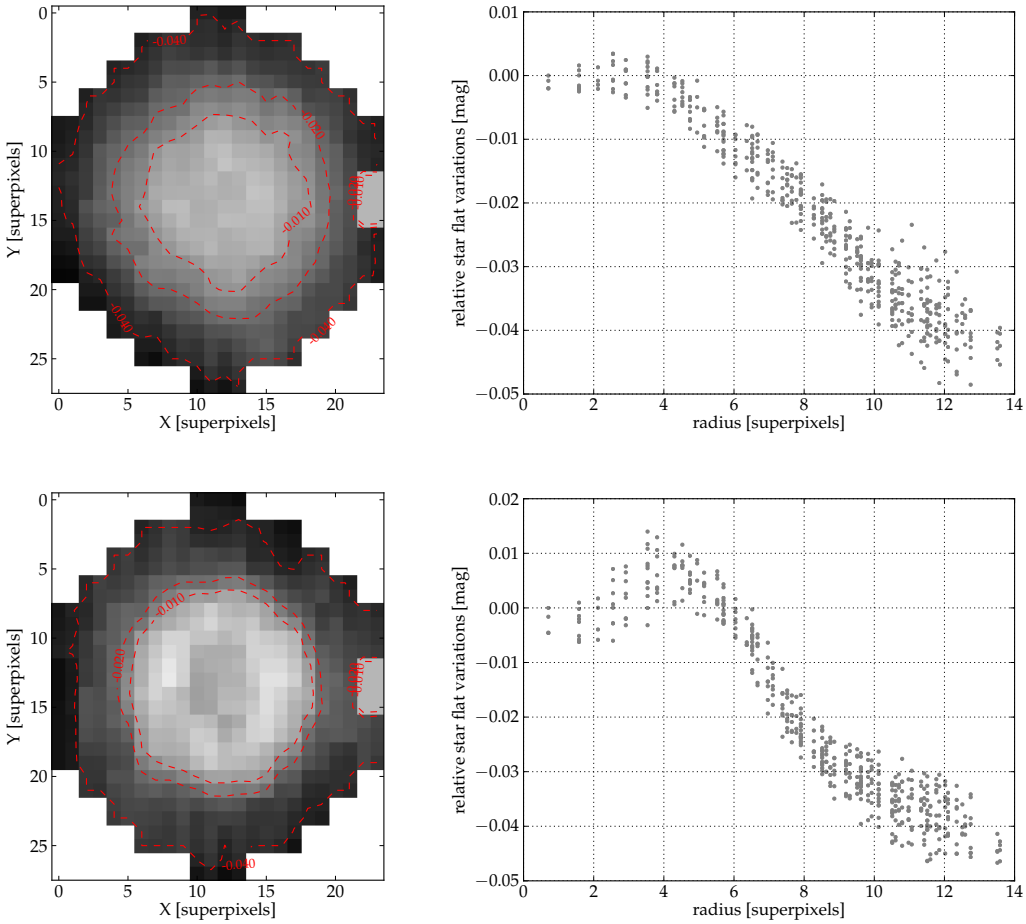

Figure 3: i-band and z-band star flats (2012-12-22)

plane (less than 1% peak-to-peak). Hence, this effect cannot explain the 2 to 7% non uniformities seen in the star flats. Ghost contamination, and maybe non-uniformities of the flat-field screen are the two next obvious explanations. But this remains to be proven.

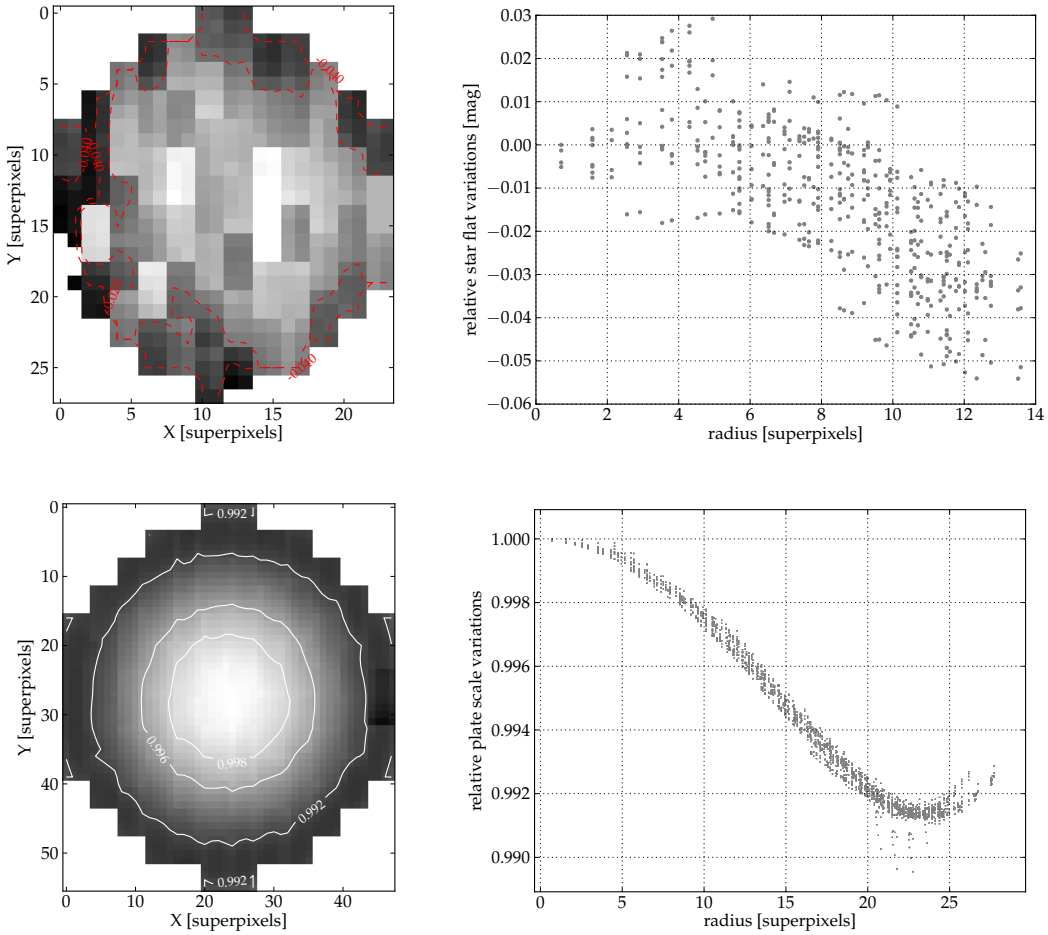

Figure 4: Up: Y-band star flat. Down: relative variations of the solid angle subtended by a camera pixel.

band	zp
g	25.296
r	25.374
i	25.379
z	25.064
Y	24.154

Table 3: Zero points applied to the measurements.

5 Testing for Filter Uniformity

We can now go ahead and start testing for potential non-uniformities of the filter edges. Such an effect is not captured by the sky or dome flats. It induces non uniformities of the imager response that depend on the object colors.

5.1 The model

If the object under study belongs to the main sequence, then, the color-dependent non-uniformities may be parameterized using simple color-terms. For example:

$$m_{\mathrm{ADU}|\mathbf{x}} = m_{\mathrm{ADU}|\mathbf{x}_0} + \delta\mathrm{zp}(\mathbf{x}) + \delta\mathrm{k}(\mathbf{x}) \times \mathrm{col}_{\mathbf{x}_0} \tag{3}$$

where $\delta\mathrm{k}(\mathbf{x})$ encodes the effect of the filter edge variations, and $\mathrm{col}_{\mathbf{x}_0}$ is the color of the star measured at a reference location (e.g. $g - i_{\mathbf{x}_0}$).

Again, since we do not know anything *a priori* about the expected shape of the δk*a*-maps, we parametrize them using superpixels, of the same size as those used to develop the δzp's. Again, this may be changed in the future. Even better, since the δk's are not expected to vary in the long term, what can be done is to use test bench measurements of the DECam filters + synthetic photometry to predict the $\delta\mathrm{k}(\mathbf{x})$ and fit only for the δzp. This will be discussed in a later iteration of this note.

Fitting the model described in equation 3 requires some more work, as we now have to measure and calibrate the color of the grid stars. Furthermore, we need to select main sequence objects, with well measured colors, which reduces by a significant amount the number of objects available, thereby increasing the star flat uncertainties.

5.2 Field star colors

We obtain the field star colors by combining the field star magnitudes ($m_{\mathbf{x}_0}$) obtained in §4 with the average zero points provided by D. Tucker and reported in table 3. Selecting stars with well measured colors requires some care, and considerably reduces the number of objects entering the fit (from XXX on average to YYY in the r-band).

The selected objects are shown in the $r - i$ vs. $g - r$ plane on figure 5. The main sequence is clearly visible. All the objects far outside the main sequence were rejected, reducing the number of objects by another. After cut, the rms of the distribution of the

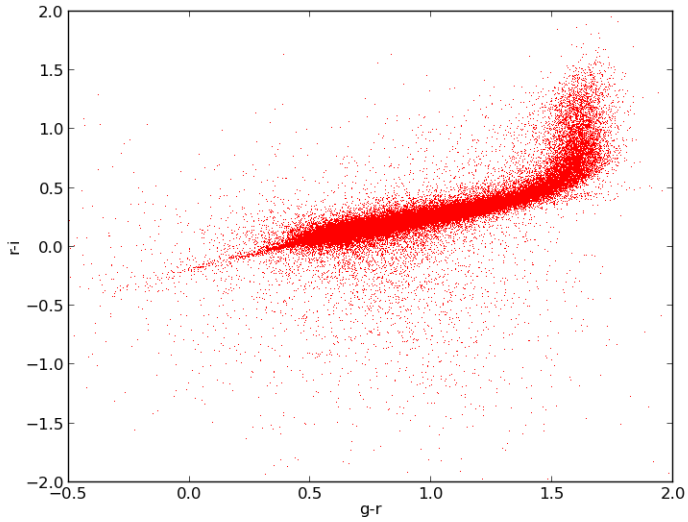

Figure 5: $r - i$ vs. $g - r$ – December field.

$g - i$ color of the final field star sample is of about 0.6 mag. (This means that we have some color lever arm).

5.3 Results

The results of the fits are presented on table 4, and on figures 6, 7 and 8. The information reported in table 4 is similar to what is shown on table 2, with one additional field, which show the gain in χ^2 when adding the δk($\mathbf{x}$) terms (it is always significant).

Figures 6, 7 and 8 show the δk($\mathbf{x}$) maps (left panels), as well as a folded version of the same maps, along a radius. As can be seen, the r, i and z bands display small but significant variations, which seem to be smooth, and could well be filter non-uniformities. It would be interesting to correlate what we see here with the manufacturer scans data (is it available ?)

Surprisingly, we don't see anything significant in the Y band. I need to know more about the red cutoff of the Y-passband to explain what I see here.

Finally, we see a clear pattern (which is also present in the November data) in the g-band. This may be due to sharp differences in the CCD QE (differences in the CCD coatings ?). Again, it would be interesting to correlate this with what can be infered from filter and CCD QE models.

date	band	N_{meas} (after cuts)	$N_{\rm pars}$	$N_\star$	χ^2/N_{dof}	$\Delta\chi^2$ (δk − no δk))
2012-11-20	g	809,943	992	82,303	10.1	-175,508
2012-11-20	r	560,781	992	82,303	9.2	-35,064
2012-11-20	i	514,690	992	82,303	10.1	-55,780
2012-11-21	z	563,646	992	82,303	3.1	-9,446
2012-11-21	Y	558,676	992	82,302	3.0	-4,996
2012-12-22	g	956,760	992	121,827	3.4	-56,953
2012-12-22	r	952,429	992	121,827	4.4	-23,732
2012-12-22	i	1,114,095	992	121,827	4.0	-86,674
2012-12-22	z	959,793	992	121,827	2.9	-9,785
2012-12-22	Y	958,393	992	121,827	2.6	-4,924

Table 4: grizY star flats.

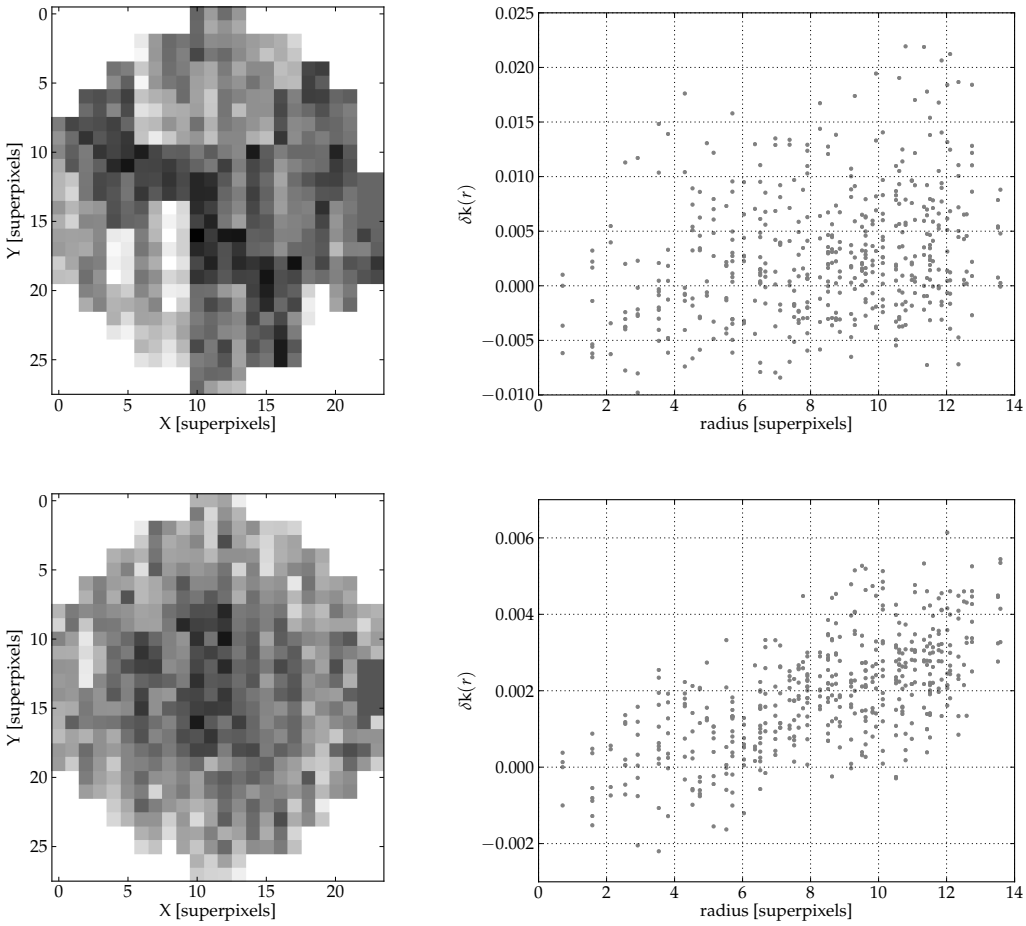

Figure 6: g-band (up) and r-band (down) star flats (2012-12-22)

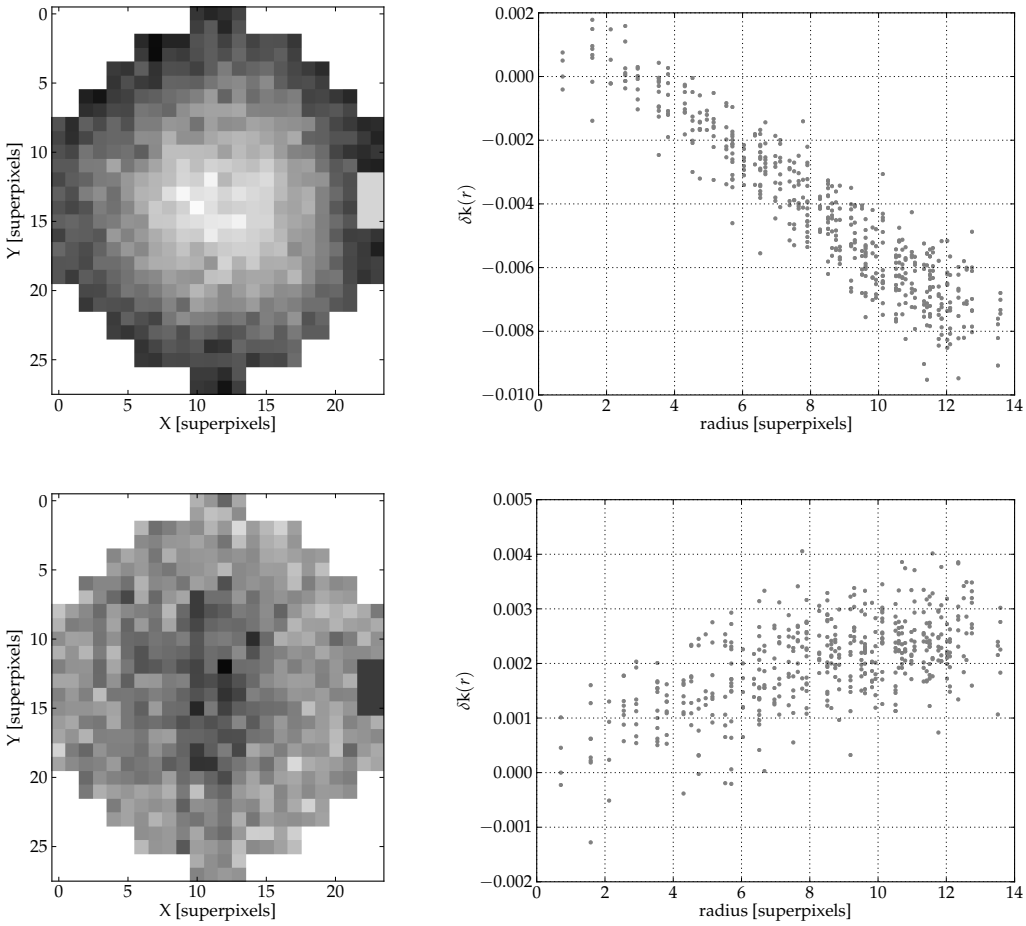

Figure 7: i-band and z-band star flats (2012-12-22)

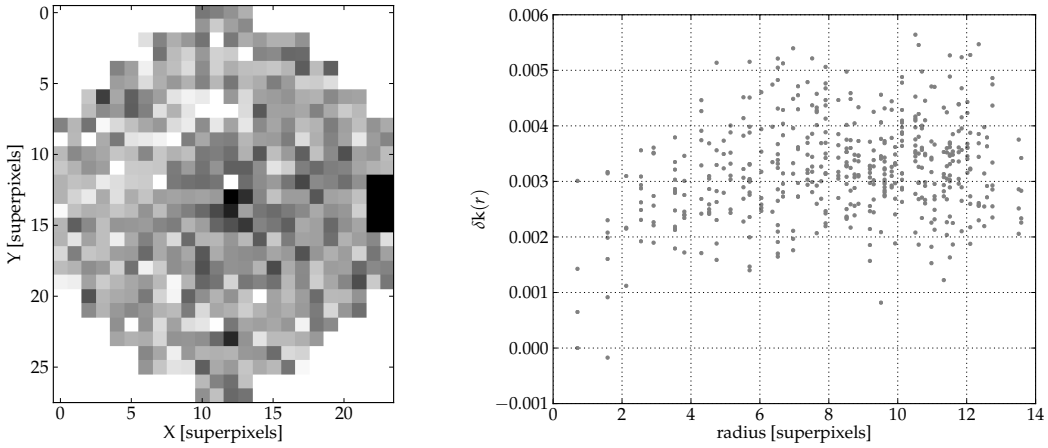

Figure 8: Up: Y-band star flat. Down: relative variations of the plate scale.

6 Stability of the dithering sequence

6.1 IQ Variations

New section.

We have checked the variations of the image quality during the dithering sequence. Figure 9 shows the variations of the average gaussian moments of the stars detected on CCD S04 as a function of the exposure number.

The figure shows clearly that the two sequences differ greatly in quality. On the november sequences, we see clear signs of star elongation (along x or y), and the image quality may vary significantly (todo: redo the november grid fit, excluding the first 8 images of the sequence. They are not dithered, but they may have an impact on the solution.) On the other hand, the december sequences, do not show any clear sign of elongation, or IQ instability (except on some g and r exposures).

6.2 Variations of the atmospheric absorption

(To be written. We allow for one zp per image.)

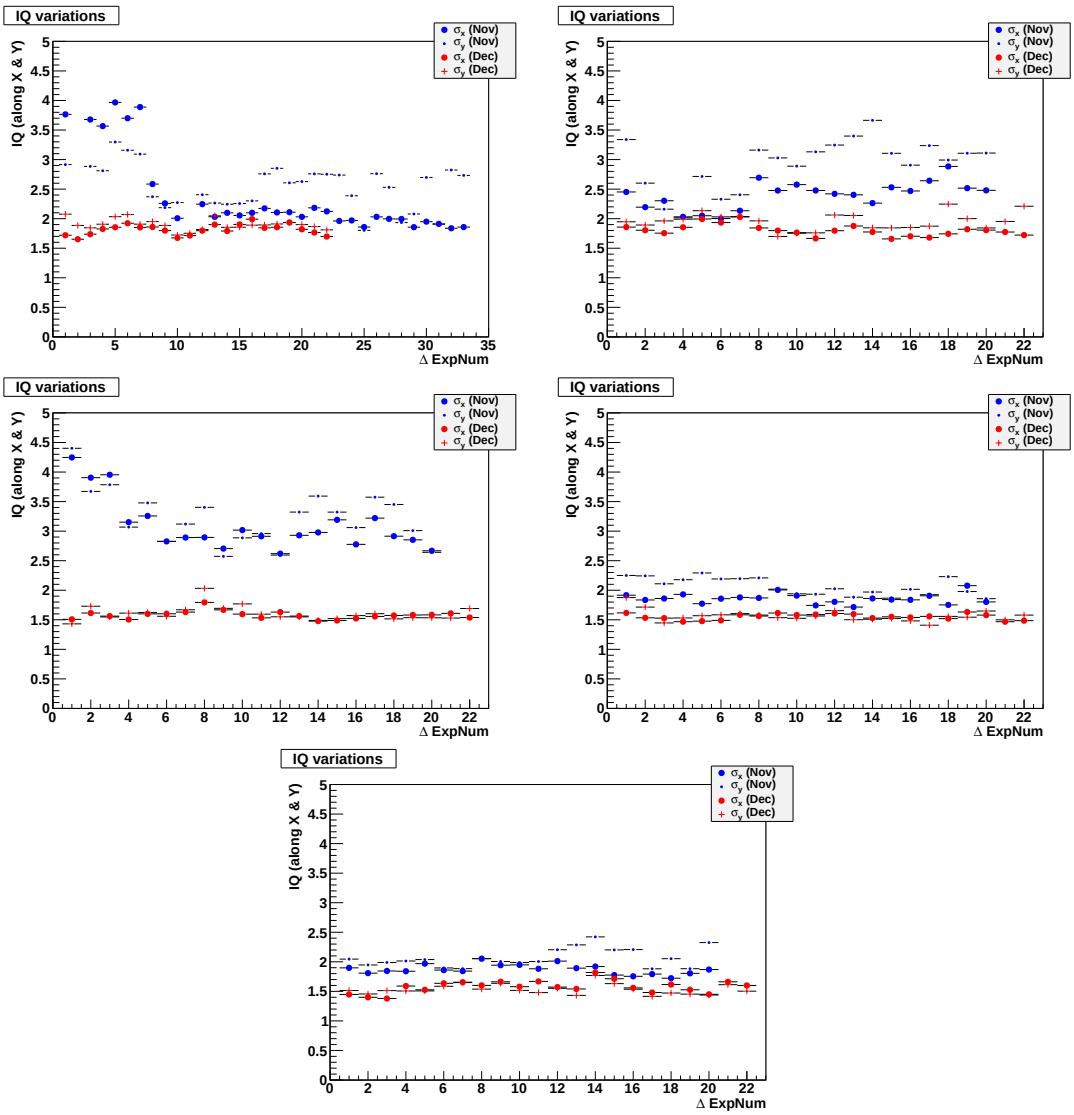

Figure 9: IQ i.e. (σ(gaussianPSF) in pixels), computed on CCD S04, as a function of the exposure number in the sequence. From left to right and top to botton: g, r, i, z and Y.

7 Stability of the star flat solution

(New section)

We have compared the two sets of star flats obtained so far, in order to assess how stable the solution is. The differences between the december and november flats are shown in figures 10 and 11. In all bands, the rms of the differences is between 0.1% and 0.3% (this number includes the noise affecting the star flat determination). However, this is not pure noise. We notice that the difference maps display spatially coherent patterns, which are, on average, of 0.2% to 0.4% (peak-to-trough).

In the g-band, the origin of the large scale effect we can see can probably be traced to the fact that the observing conditions in november were quite unstable, hence, I would not trust the november map. A simulation should allow us to assess the effects of variations in the observing conditions on the star flats.

In the other bands, we see smaller patterns, that seem to be radial. Given the size of the $\delta\mathrm{k}(\mathbf{x})$ terms, it cannot be explained by systematic differences between the colors of the november and december fields. A possible explanation, would be that the ghost pollution affecting the DECal flat fields varies slightly with the orientation of the telescope w.r.t. the screen. (It would be interesting to compare to different sets of flat fields, taken under similar conditions, but at two different dates. I'll do that one the november and december flats I have. Maybe somebody has done that already ? For example with flat fields taken on the same night ?)

A last comment on the fact that the difference between the two star flat solutions is not zero *on average*. This is a artifact of the fit as it is implemented today. Up to now, to break the degeneracies of the star flat model presented above, I chose to fix one parameter per map: the value of the map on a specific cell chosen as a reference: $\delta\mathrm{zp}(\mathbf{x}_0) = 0, \delta\mathrm{k}(\mathbf{x}_0) = 0$. The consequence of this choice, is that the maps embark the noise that affect this specific cell. In other words, if we look at the structure of the noise affecting the grid maps, we find that all the pixels are affected by a common mode (they are positively correlated). Hence, it is not surprising that two realizations of the star flats differ by some amount on average. This can be easily corrected if deemed necessary. For example, I can let all the parameters float, and add a single constraint such as $\sum \delta\mathrm{zp} = 0$ in the fit (Work in progress).

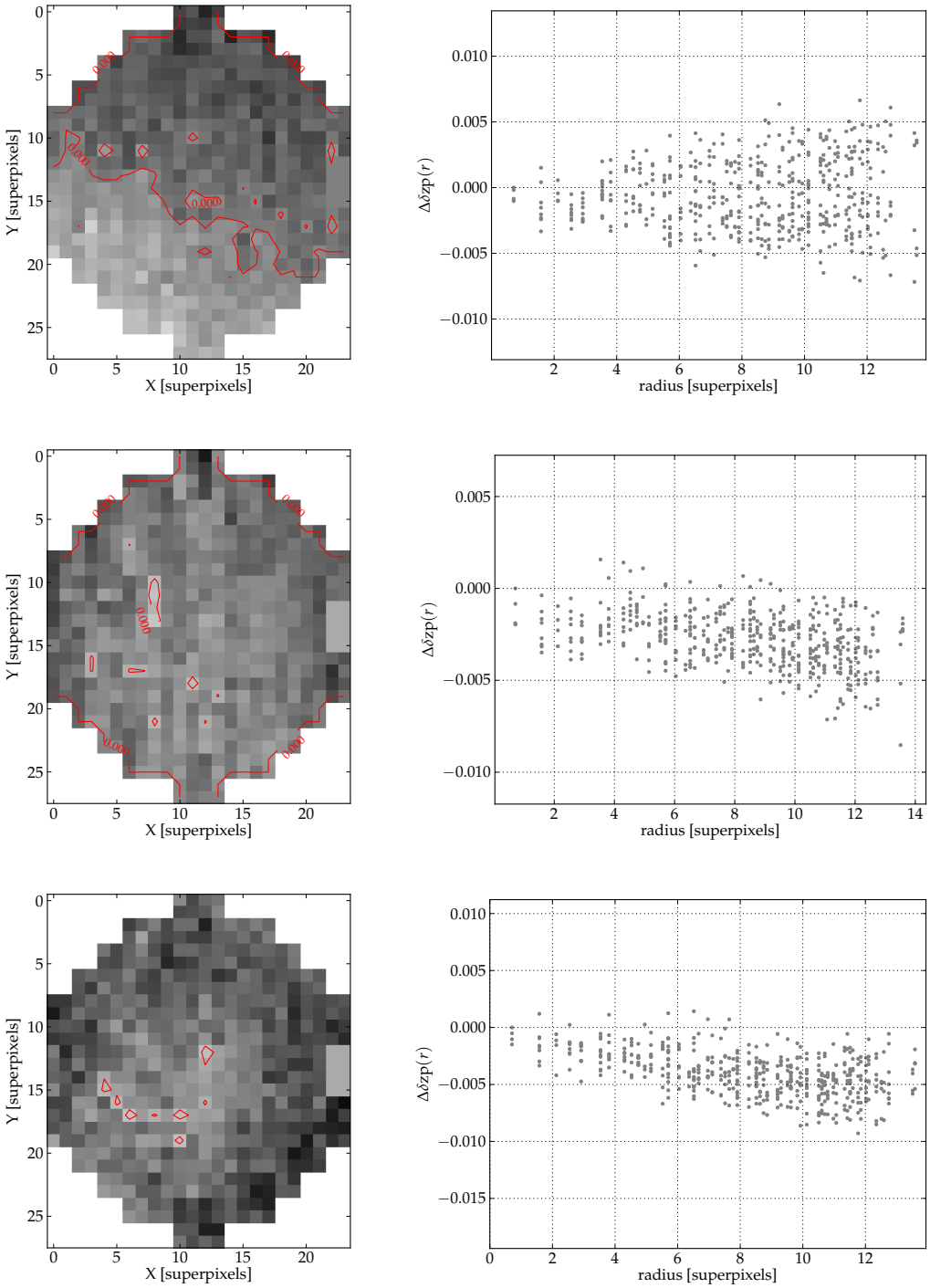

Figure 10: Differences between the december and november star flats (in the sense december - november). Upper panel: g. Middle panel: r. Lower panel: i.

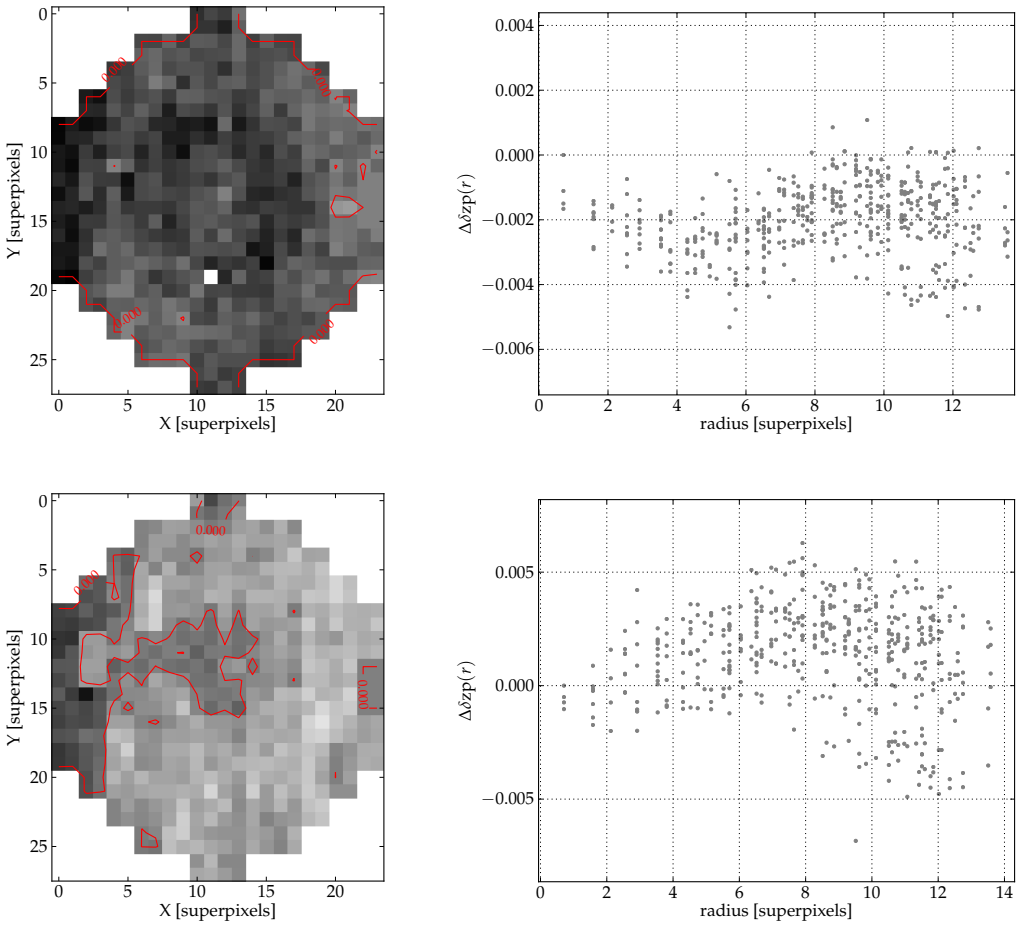

Figure 11: Differences between the december and november star flats (in the sense december - november). Upper panel: z. Lower panel: Y.

8 Work ahead

The star flat procedure seems to work. It would be good to have a few additional epochs, in order to assess how stable these maps are. Also, it would give a very good training sample to study how this procedure can be integrated into a "standard flat fielding procedure".

We detect what seems to be small variations of the filter edges accross the focal plane, as well as what may be variations in the properties of the CCD coatings (in the blue). These effects are small (but have to be accounted for if we intend to perform precision photometry). The next step on this aspect is to see whether they are present in the data provided by the filter and chip manufacturers.

The last thing is to understand the structure of these maps. The surprise (at least to me) is the imager plate scale is extremely uniform. Hence, we are dealing either ghosts, or with non-uniformities of the dome flat screen. It would be good to assess how much of each. DECal data will be extremely useful here.

References

N. Regnault, A. Conley, J. Guy, M. Sullivan, J.-C. Cuillandre, P. Astier, C. Balland, S. Basa, R. G. Carlberg, D. Fouchez, et al., Astronomy & Astrophysics **506**, 999 (2009), arXiv:0908.3808. 3

M. Betoule, J. Marriner, N. Regnault, J.-C. Cuillandre, P. Astier, and J. Guy, Astronomy & Astrophysics (2012). 3